# IMPACT OF IRREGULAR ANISOTROPIC SURFACE ROUGHNESS ON THE NEAR-WALL REGION OF TURBULENT CHANNEL FLOW

*Thomas O. Jelly and Angela Busse*

*School of Engineering, University of Glasgow, G12 8QQ, Scotland*

**thomas.jelly@glasgow.ac.uk**
**angela.busse@glasgow.ac.uk**

## Abstract

The impact of surface anisotropy upon the near-wall region of a rough-wall turbulent flow is investigated via direct numerical simulation (DNS). A set of seven irregular rough surfaces with a fixed roughness height, near-Gaussian height distributions and specified streamwise and spanwise correlation lengths were synthesised using a surface generation algorithm. By defining the *surface anisotropy ratio* (SAR) as the ratio of the streamwise and spanwise correlation lengths, we demonstrate that surfaces with a strong spanwise anisotropy (SAR $<1$) can induce an $\mathcal{O}(100\%)$ increase in the roughness function, compared to their streamwise anisotropic (SAR $>1$) equivalent. Furthermore, we find that the relationship between the roughness function $\Delta U^+$ and the SAR parameter can be fitted by an exponentially decaying function. The statistical response of the near-wall flow is studied using a "double-averaging" methodology in order to distinguish form-induced "dispersive" stresses from their turbulent counterpart. In addition, the spatial structure of the roughness layer is examined using two-point velocity correlations. Overall, the results from this study underline that the drag penalty incurred by a rough surface is strongly influenced by the surface topography and highlight its impact upon the mean momentum deficit in the outer flow.

## 1 Introduction

Many forms of irregular roughness found on engineering surfaces display some degree of anisotropy. For example, production processes, such as milling, generate irregular surfaces with a "lay" that represents the direction of predominant surface patterns (Thomas et al, 1999). Anisotropic roughness is also encountered on in-service turbine vanes (Bons et al, 2001), bio-fouled ship hulls (Monty et al, 2016) and also occurs in a geo- and astrophysical context, e.g. in the form of ripple-patterns, which for example affect sand-transporting winds on Mars (Jackson et al, 2015). As a result, the fluid dynamic properties of anisotropic forms of roughness are of great practical interest.

The drag penalty incurred by a rough surface depends on the characteristic height of the roughness features, but is also strongly influenced by the roughness topography. In a study based on surface scans, Thakkar et al (2017) identified the streamwise correlation length of the roughness as one of the key topographical parameters that influence the roughness function. Traditionally, the influence of roughness correlation length has mostly been studied for the case of regular bar-type roughness. Perry et al (1969) showed experimentally that the spacing distance between transverse bars, i.e. the effective streamwise correlation length of the surface, has a strong effect on the observed roughness effect, with short spacing giving rise to $d$-type behaviour and longer spacing inducing $k$-type behaviour. In the direct numerical simulations (DNS) of Leonardi et al (2004), the spacing of bars was shown to affect the coherence of the near-wall flow as well as the levels of turbulence anisotropy. Another widely studied form of regular anisotropic roughness are wavy walls. For example, in the experimental study of Hamed et al (2015) fundamental differences for flow over two- and three-dimensional large-scale wavy walls were found that have practical implications for bed erosion and sediment transport.

In the context of irregular roughness, Wu and Christensen (2010) studied the spatial structure of a turbulent boundary layer above a highly irregular surface replicated from a damaged turbine blade and noted an attenuation of the streamwise coherence of the near-wall flow. In a related study, Barros and Christensen (2014) reported turbulent secondary flows induced by spanwise heterogeneities over the same turbine blade roughness. However, the influence of the degree of spanwise heterogeneity, i.e. spanwise correlation length, remained unclear, as only a single roughness specimen was considered.

The objective of this study is to systematically investigate the impact of surface anisotropy upon the near-wall region of rough-wall turbulent channel flow. To this end, DNS of turbulent channel flow over a set of synthetically generated irregular rough surfaces with specified streamwise and spanwise correlation

lengths have been performed.

## 2 Surface generation algorithm

Surface heightmaps were generated by taking linear combinations of Gaussian random number matrices using a moving average (MA) process. This method of surface generation was developed by Patir (1978) and has been extended here with periodic boundaries. A periodic Gaussian heightmap, $h_{ij}$, was generated by taking the linear transformation

$$h_{ij} = \sum_{k=1}^{n}\sum_{l=1}^{m} \alpha_{kl}\eta_{rs} \qquad \begin{array}{l} i = 1, 2, \ldots, N \\ j = 1, 2, \ldots, M \\ r = [p \pmod N] + 1 \\ s = [q \pmod M] + 1 \\ p = i + k - 1 \\ q = j + l - 1 \end{array} \tag{1}$$

where $\eta_{ij}$ is an $N \times M$ matrix of uncorrelated Gaussian random numbers, $\alpha_{kl}$ are an $n \times m$ set of weights that give a user-specified autocorrelation coefficient function (ACF) and $\mathrm{mod}$ is the modulo operator.

The weights of the MA process, $\alpha_{kl}$, are determined by solving the non-linear system

$$R_{pq} = \sum_{k=1}^{n-p}\sum_{l=1}^{m-q} \alpha_{kl}\alpha_{rs} \qquad \begin{array}{l} p = 0, 1, \ldots, n-1 \\ q = 0, 1, \ldots, m-1 \\ r = k + p \\ s = l + q \end{array} \tag{2}$$

using the Newton method outlined by Patir (1978), where $R_{pq}$ is the discrete ACF. Each Gaussian heightmap is generated with an exponential ACF

$$R = \exp\left(-2.3\sqrt{\left(\frac{\Delta x_1}{\Delta x_1^*}\right)^2 + \left(\frac{\Delta x_2}{\Delta x_2^*}\right)^2}\right) \tag{3}$$

where $(\Delta x_1, \Delta x_2)$ denote the spatial separations in the streamwise and spanwise directions, respectively, and where $(\Delta x_1^*, \Delta x_2^*)$ denote the spatial separations at which the streamwise and spanwise ACF profiles decay to 10% of their values at the origin. Further details can be found in the work of Patir (1978).

Using the above method, a set of Gaussian heightmaps with systematically varied correlation lengths were generated. In total, six anisotropic surfaces and one isotropic surface were synthesised. A set of smoothly varying topographies were obtained by passing each discrete heightmap through a low-pass Fourier filter (Busse et al, 2015). The anisotropy of each filtered heightmap was quantified using the surface anisotropy ratio (SAR) defined here as

$$\mathrm{SAR} \equiv \frac{\mathcal{L}_x}{\mathcal{L}_y} \tag{4}$$

where $\mathcal{L}_x$ and $\mathcal{L}_y$ denote the streamwise and spanwise correlation lengths, respectively. Correlation lengths were computed based on a 0.2 cutoff criteria in order to be consistent with past work related to the current study (Thakkar et al, 2017). The SAR parameter is the inverse of the $S_{tr}$ parameter as defined in Thakkar et al (2017).

For the seven surfaces considered in this study, SAR ranges from 1/8 to 8. All surfaces were synthesised with a near-Gaussian height distribution, i.e. with negligible skewness ($\mathcal{S} \approx 0$) and kurtosis approximately equal to three ($\mathcal{K} \approx 3$). This allows the current study to focus on the effect of surface correlation length, since skewness and kurtosis have been effectively eliminated as parameters. Additional topographical parameters are given in table 1.

## 3 Numerical setup & averaging methods

For each surface surface listed in table 1, a DNS of turbulent channel flow with roughness on both the top and bottoms walls was performed using the iterative embedded-boundary algorithm developed by Busse et al (2015). A reference smooth-wall simulation was also performed for comparison. The flow was driven by a constant (negative) mean streamwise pressure gradient, $\Pi$, which can be used to define the mean friction velocity as $u_\tau \equiv \sqrt{(-\delta/\rho\Pi)}$ where $\delta$ denotes the mean channel half-height and $\rho$ denotes the density. The friction Reynolds number is defined here as $Re_\tau \equiv u_\tau\delta/\nu$, where $\nu$ is the kinematic viscosity. All simulations in this study were carried out at a fixed friction Reynolds number of $Re_\tau = 395$.

Throughout this work, the Cartesian velocity components, $u_i = (u_1, u_2, u_3)$, are aligned along their respective Cartesian coordinates, $x_i = (x_1, x_2, x_3)$, and $p$ denotes the fluctuating pressure. The computational domain is a rectangular volume of $(L_1 \times L_2 \times L_3)/\delta = (8.0 \times 4.0 \times 2.0)$ and is discretized using a Cartesian mesh comprised of $(N_1 \times N_2 \times N_3) = (640 \times 320 \times 576)$ grid-points. A uniform mesh spacing of $\Delta x_1^+ = \Delta x_2^+ = 4.94$ was prescribed in the streamwise and spanwise directions, whereas a non-uniform mesh with a minimum and maximum spacing of $\Delta x_{3,\min}^+ = 0.67$ and $\Delta x_{3,\max}^+ = 4.50$ was used in the wall-normal direction. All time-averaged quantities correspond to an averaging period of $T^+ = Tu_\tau^2/\nu \approx 2 \times 10^5$. In addition, approximately one thousand instantaneous three-dimensional snapshots with a viscous-scaled time separation of $\Delta T^+ = 20$ were collected for each rough-wall case. An equivalent smooth-wall dataset was also accumulated.

A double-averaging (DA) methodology (Raupach and Shaw, 1982) was employed throughout this study. For the current flow configuration, an instantaneous field variable, say $\phi$, is decomposed as

$$\phi(\mathbf{x}, t) = \langle\overline{\phi}\rangle(x_3) + \tilde{\phi}(\mathbf{x}, t) + \phi'(\mathbf{x}, t) \tag{5}$$

where $\langle\overline{\phi}\rangle$ is the DA component, $\tilde{\phi}$ is the form-induced "dispersive" fluctuation and $\phi'$ is the turbulent fluctu-

| Case | SAR | $S_a/\delta$ | $S_q/\delta$ | $\mathcal{S}$ | $\mathcal{K}$ | $\mathcal{L}_x/\delta$ | $\mathcal{L}_y/\delta$ | $ES_x$ | $ES_y$ | $S_{z,5\times5}/\delta$ | $h_{\max}/\delta$ | Line |
|---|---|---|---|---|---|---|---|---|---|---|---|---|
| $S_{81}$ | 8.000 | 0.025 | 0.031 | 0.05 | 3.01 | 0.80 | 0.10 | 0.14 | 0.43 | 0.167 | 0.11 | ···· |
| $S_{41}$ | 4.000 | 0.024 | 0.030 | 0.05 | 3.00 | 0.40 | 0.10 | 0.19 | 0.40 | 0.167 | 0.11 | -·-· |
| $S_{21}$ | 2.000 | 0.023 | 0.029 | 0.01 | 2.98 | 0.20 | 0.10 | 0.24 | 0.38 | 0.167 | 0.11 | - - - |
| $S_{11}$ | 1.000 | 0.022 | 0.028 | 0.04 | 3.02 | 0.10 | 0.10 | 0.34 | 0.34 | 0.167 | 0.11 | —— |
| $S_{12}$ | 0.500 | 0.022 | 0.027 | 0.03 | 3.08 | 0.10 | 0.20 | 0.37 | 0.23 | 0.167 | 0.11 | - - - |
| $S_{14}$ | 0.250 | 0.029 | 0.029 | 0.01 | 3.06 | 0.10 | 0.40 | 0.40 | 0.18 | 0.167 | 0.11 | -·-· |
| $S_{18}$ | 0.125 | 0.025 | 0.031 | 0.01 | 2.96 | 0.10 | 0.80 | 0.43 | 0.14 | 0.167 | 0.11 | ···· |

Table 1: Surface statistics including: Mean absolute height ($S_a$); root-mean-square (RMS) height ($S_q$); skewness ($\mathcal{S}$); kurtosis ($\mathcal{S}$); streamwise correlation length ($\mathcal{L}_x$); spanwise correlation length ($\mathcal{L}_y$); streamwise effective slope ($ES_x$); spanwise effective slope ($ES_y$); and mean peak-to-valley height ($S_{z,5\times5}$). The height of the highest roughness crest, $h_{\max}/\delta$, is also included.

ation. The DA operator is defined here as

$$\left\langle \overline{\phi} \right\rangle (x_3) = \frac{1}{\psi\,(r)} \frac{1}{L_1} \frac{1}{L_2} \int_0^{L_1} \int_0^{L_2} \overline{\phi}\,(\mathbf{x})\, \mathrm{d}x_2 \mathrm{d}x_1 \qquad (6)$$

where $\psi = A_f/\left(L_1 L_2\right)$ is ratio of the fluid-occupied area, $A_f$, to the total area $L_1 L_2$ and the overbar denotes a time-averaged quantity. Note that $\psi$ becomes less than one below the highest roughness crest ($x_3 < h_{\max}$) and that, in solid-occupied regions, $\phi\,(\mathbf{x}, t) = 0$.

Throughout this work, the roughness function, $\Delta U^+$, is defined as

$$\Delta U^+ \equiv \langle \overline{u}_1 \rangle^+_{\mathrm{cl,s}} - \langle \overline{u}_1 \rangle^+_{\mathrm{cl,r}} \qquad (7)$$

where subscripts "cl", "s" and "r" denote centre-line, smooth- and rough-wall quantities, respectively.

The root-mean-square (rms) of streamwise turbulence fluctuations, $u'_{1,\mathrm{rms}}$, is defined here as

$$u'_{x,\mathrm{rms}}\,(x_3) \equiv \sqrt{\left\langle \left(u_1\,(\mathbf{x}, t) - \overline{u}_1\,(\mathbf{x})\right)^2 \right\rangle} \qquad (8)$$

Similarly, the rms of streamwise dispersive fluctuations, $\tilde{u}_{1,\mathrm{rms}}$, is defined here as

$$\tilde{u}_{x,\mathrm{rms}}\,(x_3) \equiv \sqrt{\left\langle \left(\overline{u}_1\,(\mathbf{x}) - \langle \overline{u}_1 \rangle\,(x_3)\right)^2 \right\rangle} \qquad (9)$$

Finally, the two-point correlation of streamwise turbulence fluctuations, $R_{11}$, is defined here as

$$R_{11}\,(\Delta x_1, \Delta x_2, x_3) \equiv \frac{\left\langle \overline{u'_1\,(\mathbf{x}, t)\, u'_1\,(\mathbf{x} + \delta\mathbf{x}, t)} \right\rangle}{\left(u'_{1,\mathrm{rms}}(x_3)\right)^2} \qquad (10)$$

where the streamwise-spanwise separation vector is $\delta\mathbf{x} = (\Delta x_1, \Delta x_2, 0)$.

## 4 Results

The roughness function, $\Delta U^+$ (equation 7), is plotted as a function of the SAR parameter (equation 4) in figure 1. A striking observation based on this data is that $\Delta U^+$ exhibits an $\mathcal{O}\,(100\%)$ increase as SAR is decreased from 8 to 1/8. Considering that all surfaces have been scaled to an identical mean peak-to-valley height and share near-Gaussian height distributions (see table 1), the sharp rise in $\Delta U^+$ underlines the impact that surface anisotropy can have upon the drag penalty incurred by a rough surface.

Furthermore, the relationship between $\Delta U^+$ and the SAR parameter shown in figure 1 can be expressed as an exponential function of the form

$$\Delta U^+ = b_1 + b_2 \exp\left(-b_3 \mathrm{SAR}\right) \qquad (11)$$

where $\{b_1, b_2, b_3\} = \{3.14, 4.65, 0.28\}$. Using equation 11, the roughness function is predicted to obtain a minimum value of $\Delta U^+ \approx 3.14$ as SAR $\to \infty$ and a maximum value of $\Delta U^+ \approx 7.79$ as SAR $\to 0$.

Thakkar et al (2017) identified $\mathcal{L}_x$ as one of the key topographical parameters influencing the roughness function based on data obtained from DNS over a range of rough surfaces based on scans. The numerically generated irregular rough surfaces of the current study allow a more systematic probing of the influence of the correlation length. The strong decrease in $\Delta U^+$ with increasing SAR $> 1$ confirms the findings of Thakkar et al (2017) regarding $\mathcal{L}_x$. Based on the current results we can in addition show that $\mathcal{L}_y$ also affects the roughness function as shown by the increase of $\Delta U^+$ with decreasing SAR $< 1$. However, with reference to figure 1, it is clear that the streamwise correlation length $\mathcal{L}_x$ of a surface has considerably stronger influence on the fluid dynamic roughness effect than its spanwise correlation length $\mathcal{L}_y$.

Wall-normal profiles of the DA streamwise velocity normalised by the friction velocity are plotted in figure 2. As the SAR parameter increases, the downward shift of the log-law decreases — indicating that spanwise anisotropic surfaces (SAR $\to 0$) induce the largest rise in the mean momentum deficit. Below the highest roughness crest ($x_3 < h_{\max}$), a DA reverse flow forms within the canopy of each surface (see inset figure 2). Whilst the shape and strength of the reverse flow region is strongly affected by the levels of streamwise anisotropy (SAR $> 1$), a relative insen-

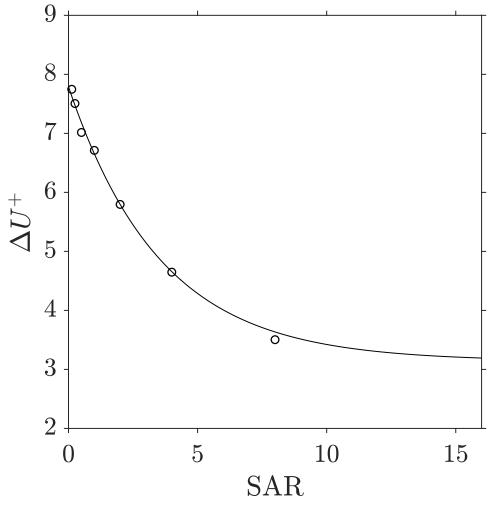


Figure 1: The roughness function, $\Delta U^+$, plotted as a function of the SAR parameter. An exponential behaviour (equation 11) can be fitted to the data (——).

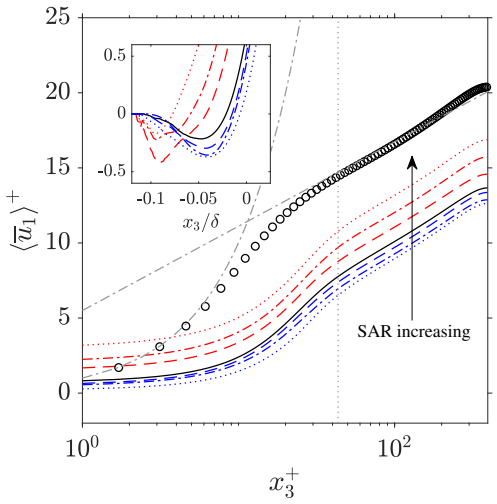


Figure 2: Mean streamwise velocity profiles. Line-types are given in table 1. Smooth wall data (○) is also included. The smooth-wall viscous sublayer, $\langle \overline{u}_1 \rangle^+ = x_3^+$, and the log-law, $\langle \overline{u}_1 \rangle^+ = \kappa^{-1} \ln x_3^+ + B$, with $\kappa = 0.41$ and $B = 5.5$, are also plotted (- - - -). The highest roughness crest is shown as the vertical dotted line (· · · ·).

sitivity is observed for spanwise anisotropic surfaces (SAR $< 1$).

Wall-normal profiles of the DA streamwise velocity-defect normalised by the friction velocity are shown in figure 3. Above the highest roughness crest ($x_3 > h_{\max}$), a good collapse between the smooth- and rough-wall data is observed indicating similarity in the outer layer mean flow. These results provide evidence for Townsend's outer similarity hypothesis (Townsend 1976) and agree with the findings of past numerical (Busse and Sandham, 2017) and experimental (Flack and Schultz, 2014) studies.

Wall-normal profiles of the RMS streamwise turbulence fluctuations, $u'_{1,\text{rms}}$ (equation 8), normalised by the friction velocity are plotted figure 4. The smooth- and rough-wall RMS profiles collapse in the outer region and, with reference to the data shown previously in figure 3, provide additional evidence for Townsend's outer similarity hypothesis. For each surface considered in this study, the maximum $u'_{1,\text{rms}}$ occurs below the highest roughness crest and exhibits a significant suppression relative to the smooth-wall value. An attenuation of the peak value of $u'_{1,\text{rms}}$ in the presence of surface roughness can be interpreted as a disruption of the near-wall turbulence cycle (Schultz & Flack, 2007). Considering that the suppression of peak $u'_{1,\text{rms}}$ increases as SAR decreases (see figure 4), the current results imply that spanwise anisotropic surfaces are more effective at interrupting the near-wall streaks and quasi-streamwise vortices. Finally, we note that appreciable levels of $u'_{1,\text{rms}}$ persist deep within the roughness canopy of each surface (see inset figure 4) and that streamwise turbulence activity is promoted with increasing SAR. This trend agrees well the past results of Thakkar et al (2017), who

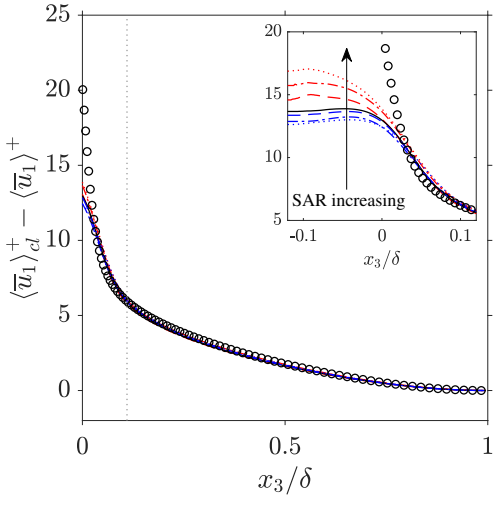


Figure 3: Velocity-defect profiles. Line-types are given in table 1. Smooth wall data (○) is also included. The highest roughness crest is shown as the vertical dotted line (· · · ·).

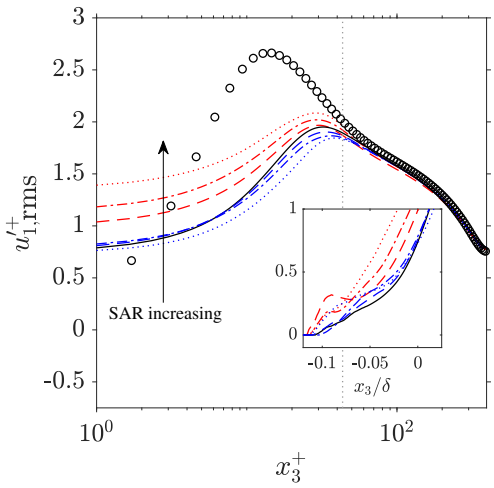


Figure 4: RMS streamwise turbulence intensity profiles. Line-types are given in table 1. Smooth wall data ($\circ$) is also included. The highest roughness crest is shown as the vertical dotted line ($\cdots$).

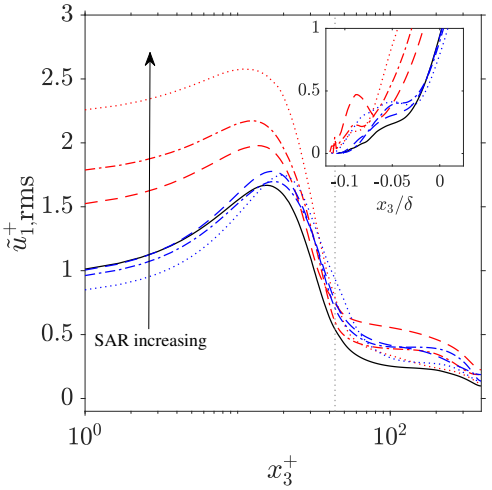


Figure 5: RMS streamwise dispersive intensity profiles. Line-types are given in table 1. Smooth wall data ($\circ$) is also included. The highest roughness crest is shown as the vertical dotted line ($\cdots$).

noted elevated turbulence kinetic energy (TKE) levels below the highest peak of an irregular surface with SAR $\approx 30$, relative to a surface with SAR $\approx 1/30$.

Wall-normal profiles of the RMS streamwise dispersive fluctuations, $\tilde{u}_{1,\mathrm{rms}}$ (equation 9), normalised by the friction velocity are shown in figure 5. Above the highest roughness crest ($x_3 > h_{\max}$), the magnitude of $\tilde{u}_{1,\mathrm{rms}}$ is appreciably lower than its turbulent counterpart (see figure 4) and shows no obvious dependence upon the SAR parameter. In contrast, below the highest roughness crest, the magnitudes of $\tilde{u}_{1,\mathrm{rms}}$ and $u'_{1,\mathrm{rms}}$ become comparable as a result of increasing spatial heterogeneity in the time-averaged flow. Comparing the $\tilde{u}_{1,\mathrm{rms}}$ profiles, it is clear that greater heterogeneity prevails within the canopies of streamwise anisotropic rough surfaces. One possible explanation for this behaviour is a "streamwise-channeling" effect whereby regions of high-speed time-averaged axial velocity (i.e. high relative to the local DA value) are free to develop within the elongated cavities of streamwise anisotropic surfaces. Such channeling mechanisms may not occur in the case of spanwise anisotropic surfaces since the flow is more likely to "skim" past the closely-spaced roughness cavities in a $d$-type manner (Perry et al, 1969).

In order to complement the single-point streamwise velocity statistics shown in figures 2, 3, 4 and 5, the two-point correlation of streamwise turbulence velocity fluctuations, $R_{11}$ (equation 10), was also evaluated and examined. Contours of $R_{11}$ plotted five wall-units above the highest roughness crest of surfaces $\mathrm{S}_{81}$ and $\mathrm{S}_{18}$ are compared in figure 6. Whilst the spanwise width of the contours above both surfaces compare well, their streamwise length show a clear dependence on the SAR parameter. For example, at a correlation level of 0.1, the streamwise extent of $R_{11}$ is approximately 30% shorter above the spanwise-anisotropic surface than that of the streamwise-anisotropic case. Considering that the elongated streamwise extent of $R_{11}$ is linked to the organisation of large-scale turbulent motions (Wu and Christensen, 2010), figure 6 highlights the impact that surface anisotropy has upon the turbulence structure within the roughness layer.

## 5 Discussion

DNS of rough-wall turbulent channel flow over synthetically generated irregular surfaces with specified correlation lengths were performed at a friction Reynolds number of 395. The ratio of the streamwise and spanwise correlation lengths was used to define the *surface anisotropy ratio* (SAR) parameter. Seven surfaces were considered: an isotropic surface (SAR $= 1$), three streamwise-anisotropic surfaces (SAR $> 1$) and three spanwise-anisotropic surfaces (SAR $< 1$). The aim of this work was to investigate the impact of irregular anisotropic surface roughness on the near-wall turbulent flow.

For the surfaces considered so far in this study, the roughness function, $\Delta U^+$, exhibits an $\mathcal{O}(100\%)$ increase from 3.62 to 7.75 as the SAR parameter is decreased from 8 to 1/8 (figure 1). Considering that each surface has a near-Gaussian height distribution and the same mean peak-to-valley height (table 1), the sensitivity of $\Delta U^+$ with respect to the SAR parameter underlines the strong effect that surface anisotropy has upon determining the momentum deficit in the outer flow. We find that $\Delta U^+$ decreases approximately exponentially with increasing SAR (figure 1) over the range of SAR investigated.

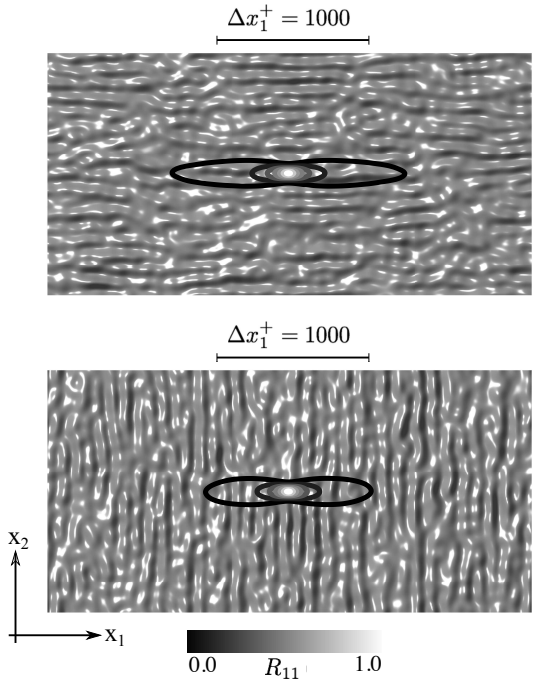


Figure 6: Two-point axial velocity correlation contours, $R_{11}\,(\Delta x_1, \Delta x_2)$, evaluated five wall units above the highest roughness crest of (a) surface $S_{81}$ and (b) surface $S_{18}$.

In the present work, the statistical response of the near-wall flow was examined in the context of single- and two-point statistics of streamwise velocity. A double-averaging methodology was adopted in order to delineate the statistical contributions of "form-induced" dispersive fluctuations and their turbulent counterpart (equation 5). Preliminary observations from this study include: (i) Outer similarity is observed on both first-order and second-order single-point statistics (figures 3 and 4); (ii) relative to the smooth-wall case, the peak value of RMS turbulent fluctuations becomes most suppressed for spanwise anisotropic surfaces (figure 4); (iii) changes in the RMS dispersive streamwise fluctuations are confined below the highest roughness crest, where the peak value increases with increasing streamwise surface anisotropy (figure 5) and (iv) the streamwise extent of the two-point correlation of streamwise velocity is significantly shorter above spanwise anisotropic surfaces, compared to their streamwise anisotropic counterpart (figure 6).

Further results will be discussed, including the relative magnitude of dispersive and Reynolds shear stresses and their sensitivity with respect to the SAR parameter. Results from additional simulations with more extreme levels of surface anisotropy (SAR=1/16 and SAR=16) will also be presented.

## Acknowledgments

This work was funded by EPSRC grant EP/P004687/1. Compute time on the ARCHER facility (http://www.archer.ac.uk) via the UK Turbulence Consortium (EPSRC grant EP/L000261/1) and ARCHIE-WeSt High Performance Computer (www.archie-west.ac.uk) (EPSRC grant EP/K000586/1) are gratefully acknowledged.

## References

Barros, J. M. and Christensen, K. T. (2014), Observations of turbulent secondary flows in a rough-wall boundary layer, *J. Fluid Mech.* **748**, R1.

Bons, J. P., Taylor, R. P., McClain S. T., and Rivir, R. B. The many faces of turbine surface roughness, *J. Turbomach.*, **123** 730–748.

Busse, A., Lützner, M., and Sandham, N. D. (2015), Direct numerical simulation of turbulent flow over a rough surface based on a surface scan, *Comp. Fluids*, **116**, 129-147.

Busse, A., Thakkar, M., and Sandham, N. D. (2017), Reynolds-number dependence of the near-wall flow over irregular rough surfaces, *J. Fluid Mech.* **810**, 196-224.

Flack, K. A. and Schultz, M. P. (2014), Roughness effects on wall-bounded turbulent flows, *Phys. Fluids* **26**, 101305.

Hamed, A. M., Kamdar, A., Xastillo, L., and Chamorro, L. P. (2015), Turbulent boundary layer over 2D and 3D large-scale wavy walls, *Phys. Fluids.* **27**, 106601.

Jackson, D. W. T., Bourke, M.C., and Smyth, T. A. G. (2015), The dune effect on sand-transporting winds on Mars, *Nature Comm.* **6**, 8796.

Leonardi, S., Orlandi, P., Djenidi, L. and Antonia, R. A. (2004), Structure of turbulent channel flow with square bars on one wall, *Int. J. Heat Fluid Flow* **25**, pp. 384–392.

Monty, J. P., Dogan, E., Hanson R., Scardino, A. J., Ganapathisubramani, B. and Hutchins, N. (2016), An assessment of the ship drag penalty arising from light calcareous tubeworm fouling, *Biofouling* **32**, 451-464.

Napoli, E., Armenio, V. and De Marchis, M. (2008), The effect of slope of irregularly distributed roughness elements on turbulent wall-bounded flows, *J. Fluid Mech.* **613**, 385-394.

Patir, N. (1978), A numerical procedure for random generation of rough surfaces, *Wear* **47** 263-277.

Perry, A. E., Schofield, W. H. and Joubert, P. N. (1969), Rough wall turbulent boundary layers, *J. Fluid Mech.* **37**, 383-413.

Raupach, M. R. and Shaw, R. H. (1982), Averaging procedures for flow within vegetation canopies, *Bound.-Layer Meteor.* **22**, 79-90.

Schultz, M. P. and Flack, K. A. (2007), The rough-wall turbulent boundary layer from the hydraulically smooth to the fully rough regime, *J. Fluid Mech.* **580**, 381-405.

Thakkar, M., Busse, A. and Sandham, N. D. (2016), Surface correlations of hydrodynamic drag for transitionally rough engineering surfaces, *J. Turbul.* **18**, 138-169.

Thakkar, M., Busse, A. and Sandham, N. D. (2018), Direct numerical simulation of turbulent channel flow over a surrogate for Nikuradse-type roughness, *J. Fluid Mech.* **837**, R1.

Thomas, T. R., Rosén, B. G. and Amini N. (1999), Fractal characterisation of the anisotropy of rough surfaces, *Wear* **232**, 41-50.

Wu, Y. and K. T. Christensen (2010), Spatial structure of a turbulent boundary layer with irregular surface roughness, *J. Fluid Mech.* **655**, 380–418.